Influence of computational aspects on simulations of a turbulent jet diffusion flame

Bart Merci and Erik Dick
Department of Flow, Heat and Combustion Mechanics, Ghent University, Ghent, Belgium

Received July 2002
Revised November 2002
Accepted January 2003

Keywords *Turbulence, Thermal diffusion, Jets*

Abstract *The influence of computational aspects on simulation results is quantitatively investigated for the specific case of a turbulent piloted jet diffusion flame (Sandia Flame D). It is illustrated that, with a fixed turbulence and chemistry model, the results can heavily depend on the numerical aspects. The influence of inlet boundary conditions has already been discussed in an earlier paper. In this work, attention is focused onto the order of accuracy of the spatial discretization in the numerical scheme and onto the position of the outlet boundary. It is stressed that the purpose is not to judge the quality of the applied models, but to illustrate the possible impact of numerical influence factors. The conclusion is a warning message and a demonstration that all numerical aspects must be completely described when calculation results are presented.*

1. Introduction

In many papers, results of numerical simulations are compared with the experimental data. Often, all differences between the computed and measured values are blamed on the employed models. However, as pointed out by Pope (2000), there may be many different contributions to the observed discrepancies.

First, there is an uncertainty in the experimental data. Only when results are compared with DNS reference data, this contribution to the global discrepancy can be ignored (although there may still be some error due to averaging or lack of statistical accuracy). Secondly there may be differences in the boundary conditions of the experiment and simulation. Next, the governing equations must be solved. A numerical error is inevitably introduced. Finally, there is the inaccuracy of the used models. This paper mainly focuses on the influence of boundary conditions and numerical accuracy.

For that purpose, the numerical simulation of a turbulent piloted jet diffusion flame is studied (Sandia Flame D) (Barlow and Frank, 1998). The turbulence model is the standard $k - \varepsilon$ model (Jones and Launder, 1972), with an adjusted model constant $c_{\varepsilon 2} = 1.8$. A pre-assumed β-probability density function (PDF) approach is used within the conserved scalar framework.

The first author works as Postdoctoral Fellow of the Fund for Scientific Research – Flanders (Belgium) (F.W.O. – Vlaanderen).

International Journal of Numerical Methods for Heat & Fluid Flow
Vol. 13 No. 7, 2003
pp. 887-898

0961-5539
DOI 10.1108/09615530310502082

Standard equations and model constants are used. The chemistry model is a simplified version of the constrained equilibrium model (Bilger and Starner, 1983), as described in Merci *et al.* (2001). All these models are fixed, so that the differences in numerical results are independent of the model choices.

2. Model description

The standard $k-\varepsilon$ model is used as the turbulence model. The turbulent stresses in the RANS equations are modelled as:

$$\tau_{ij}^{\mathrm{T}} = -\bar{\rho}\widetilde{v_i''v_j''} = 2\mu_{\mathrm{t}}S_{ij} - \frac{2}{3}\rho k\delta_{ij}, \tag{1}$$

where the turbulent or "eddy" viscosity is defined as:

$$\mu_{\mathrm{t}} = \rho c_{\mu} k \tau_{\mathrm{t}}, \tag{2}$$

with the model constant $c_{\mu} = 0.09$. Favre averages are used. The turbulent time scale τ_{t} is defined in a high-Reynolds formulation (standard):

$$\tau_{\mathrm{t}} = \frac{k}{\varepsilon}. \tag{3}$$

The steady-state transport equations for the turbulence quantities are (Merci *et al.*, 2001):

$$\begin{cases} \dfrac{\partial}{\partial x_k}(\rho k v_k) = \tau_{ik}^{\mathrm{T}}\dfrac{\partial v_k}{\partial x_i} - \rho\varepsilon + \dfrac{\partial}{\partial x_k}\left[\left(\mu + \dfrac{\mu_{\mathrm{t}}}{\sigma_k}\right)\dfrac{\partial k}{\partial x_k}\right] - \dfrac{\mu_{\mathrm{t}}}{\rho^2}\dfrac{\partial \rho}{\partial x_i}\dfrac{\partial p}{\partial x_i} \\ \dfrac{\partial}{\partial x_k}(\rho\varepsilon v_k) = \left(c_{\varepsilon 1}\tau_{ik}^{\mathrm{T}}\dfrac{\partial v_k}{\partial x_i} - c_{\varepsilon 2}f_2\rho\varepsilon - c_{\varepsilon 3}\dfrac{\mu_t}{\rho^2}\dfrac{\partial \rho}{\partial x_i}\dfrac{\partial p}{\partial x_i}\right)\dfrac{1}{\tau_{\mathrm{t}}} + \dfrac{\partial}{\partial x_k}\left[\left(\mu + \dfrac{\mu_{\mathrm{t}}}{\sigma_{\varepsilon}}\right)\dfrac{\partial_{\varepsilon}}{\partial x_k}\right], \end{cases} \tag{4}$$

with the model constants $\sigma_k = 1$, $c_{\varepsilon 1} = 1.44$, $c_{\varepsilon 2} = 1.8$, $c_{\varepsilon 3} = 1$ and $\sigma_{\varepsilon} = 1.3$. The value $c_{\varepsilon 2} = 1.8$ differs from the standard value 1.92 (since it is claimed in http://www.ca.sandia.gov/tdf/Workshop/Submodels.html that this ensures the correct spreading rate for the studied flame). However, this point is discussed later in this paper.

For the modelling of turbulence-chemistry interaction, a pre-assumed β-PDF is used, with the conserved scalar approach. The steady-state transport equations for the mean mixture fraction and its variance are (Merci *et al.*, 2001):

$$\begin{cases} \dfrac{\partial}{\partial x_j}(\rho\xi v_j) = \dfrac{\partial}{\partial x_j}\left[\left(\rho D + \dfrac{\mu_{\mathrm{t}}}{\sigma_{\xi}}\right)\dfrac{\partial \xi}{\partial x_j}\right] \\ \dfrac{\partial}{\partial x_j}(\rho g v_j) = \dfrac{\partial}{\partial x_j}\left[\left(\rho D + \dfrac{\mu_{\mathrm{t}}}{\sigma_g}\right)\dfrac{\partial g}{\partial x_j}\right] + 2\dfrac{\mu_{\mathrm{t}}}{\sigma_{\xi}}\dfrac{\partial \xi}{\partial x_j}\dfrac{\partial \xi}{\partial x_j} - c_g\rho g\dfrac{1}{\tau_{\mathrm{t}}}, \end{cases} \tag{5}$$

with standard values for the model constants: $\sigma_{\xi} = \sigma_g = 0.7$ and $c_g = 2$.

A simplified version of the constrained equilibrium (Bilger and Starner, 1983) is used as chemistry model (Merci *et al.*, 2001). Thermochemical properties are tabulated *a priori* and looked up during the calculations, with the program FLAME (Merci *et al.*, 2001).

3. Experimental setup

The geometry of the test case (Sandia "Flame D") studied experimentally at Sandia National Laboratories and Darmstadt University of Technology, is completely described by Barlow and Frank (1998). A central fuel jet – 75 per cent air and 25 per cent methane by volume – is surrounded by a coflow air stream. The unconfined flame is stabilized by a high-temperature pilot stream (around 1,900 K) between the jet and the coflow. The bulk velocities of the central jet, pilot stream and coflow air are 49.6, 11.4 and 0.9 m/s, respectively. The Reynolds number of the central fuel jet, based on mean velocity U_{m} and central nozzle diameter D_{n} is $\mathrm{Re} = \rho U_{\mathrm{m}} D_{\mathrm{n}}/\mu = 22,400$.

4. Computational grid and boundary conditions

The basic computational grid ($140D_{\mathrm{n}} \times 25D_{\mathrm{n}}$) consists of 113×89 nodes. The central fuel jet radially contains 16 cells and the pilot stream 24 cells. Stretching is applied towards the outer boundary. Axially, the first cell size is equal to the radial size of the cells in the fuel jet and stretching is applied towards the outlet. Results are also presented for another grid ($80D_{\mathrm{n}} \times 25D_{\mathrm{n}}$), in which the outlet boundary is closer to the nozzle exit. Grid independence of the results is investigated by refining the basic grid (225×177 grid points).

At the inlet boundary, the velocity components and turbulent kinetic energy are prescribed as measured at Darmstadt University of Technology (http://www.ca.sandia.gov/tdf/Workshop/Submodels.html). Static pressure is extrapolated from the flow field. For the central fuel jet, the mixture fraction is set to $\xi = 1$, while in the coflow air stream $\xi = 0$. The pilot stream has a mixture fraction $\xi = 0.27$ (see http://www.ca.sandia.gov/tdf/Workshop/Submodels.html). The mixture fraction variance is set equal to zero at the inlet. Finally, the dissipation rate ε must be determined. A complete discussion on this aspect is found in the work of Merci *et al.* (2002), where two acceptable methods are obtained. In the first method, the measured profiles for the mean velocity components and turbulent kinetic energy are imposed, and the ε transport equation (4) is solved under the assumption of fully developed flow conditions (axial derivatives set to zero). At solid boundaries, ε is determined as:

$$\varepsilon_w = 2\frac{\mu}{\rho}\left(\frac{\partial\sqrt{k}}{\partial n}\right)^2, \tag{6}$$

with n the unity vector normal to the boundary. The required time for the additional computation with this method is short, since the equation has to be

solved only on one grid line. The advantages are that the method can easily be applied to any inlet geometry (be it a central jet, an annulus flow or a coflow), and that the obtained ε profile is consistent with the $k - \varepsilon$ model in the actual simulation.

An alternative method is to determine ε from a mixing length, as suggested by Jones (1994):

$$\varepsilon = \frac{c_\mu^{3/4} k^{3/2}}{l_\mathrm{m}}, \tag{7}$$

where the measured profile for k has to be introduced. The problem is then shifted to the determination of a suitable profile for the mixing length l_m. In the work of Merci *et al.* (2002), the following expression is suggested:

$$\frac{l_\mathrm{m}}{D_\mathrm{h}} = (1 - \exp(-2 \times 10^6 (y/D_\mathrm{h})^3))(1/15 - (1/2 - y/D_\mathrm{h})^4), \tag{8}$$

where y is the normal distance from the nearest solid boundary and D_h is the hydraulic diameter.

In this work, the first method has been used to determine the ε inlet profile.

At the axis, symmetry conditions are imposed: radial derivatives are set equal to zero for all quantities, except for the radial velocity component (which is set equal to zero). At the outlet and side boundary, the axial derivatives are set to zero for all quantities, except for static pressure, which is prescribed to be atmospheric.

5. Influence of different aspects

As mentioned earlier, the aim of the paper is not the comparison of numerical results to the experimental data, but rather a comparison between the numerical results themselves, without judgement of the applied models.

5.1 Numerical scheme

The accuracy of the numerical scheme is very important. Comparisons are made between the results obtained with a first-order upwind scheme for the convective fluxes, and results obtained with a second-order accurate upwinding. The latter is a second-order accurate AUSM-like upwind scheme, fully described in Merci *et al.* (2000) and Vierendeels *et al.* (2001) for non-reacting flows. It is readily extended for reacting flows. For convective fluxes, velocity upwinding is applied, with values at the cell faces extrapolated with the van Leer-κ method. The value $\kappa = 1/3$ is chosen, so that the third order accuracy is obtained on an equidistant orthogonal grid (and second-order accuracy on more general grids). The acoustic and viscous fluxes are discretized centrally (second-order accurate). Artificial numerical dissipation for pressure is added into the mass flux in order to avoid pressure wiggles in the steady-state solution. This dissipation is small and well controlled. When a first-order accurate upwind scheme is used for the convective fluxes, it must be

kept in mind that the numerical artificial dissipation is also introduced, simply by the discretization. The dissipation can be large and is basically uncontrollable. As mentioned by Pope (2000), the leading order truncation error in one-dimensional convection-diffusion equation is equivalent to an additional viscous term, with "numerical" viscosity:

$$\mu_{\text{num}} = \frac{1}{2}\rho U h, \tag{9}$$

where h is the grid spacing.

In Figure 1, profiles are shown for the mean velocity and mixture fraction on the symmetry axis. Their inverses are also shown, in order to focus on the final decay. The impact of the order of accuracy of the numerical scheme is important. Large differences occur for $x/D_{\text{n}} > 20$ in the mean velocity, and consequently also in the mean mixture fraction profiles. The reason is the uncontrolled large numerical artificial dissipation near the inlet boundary when first-order upwinding is used for the convective fluxes. Indeed, due to the high velocity for small x, and the relatively low value of the eddy viscosity, the

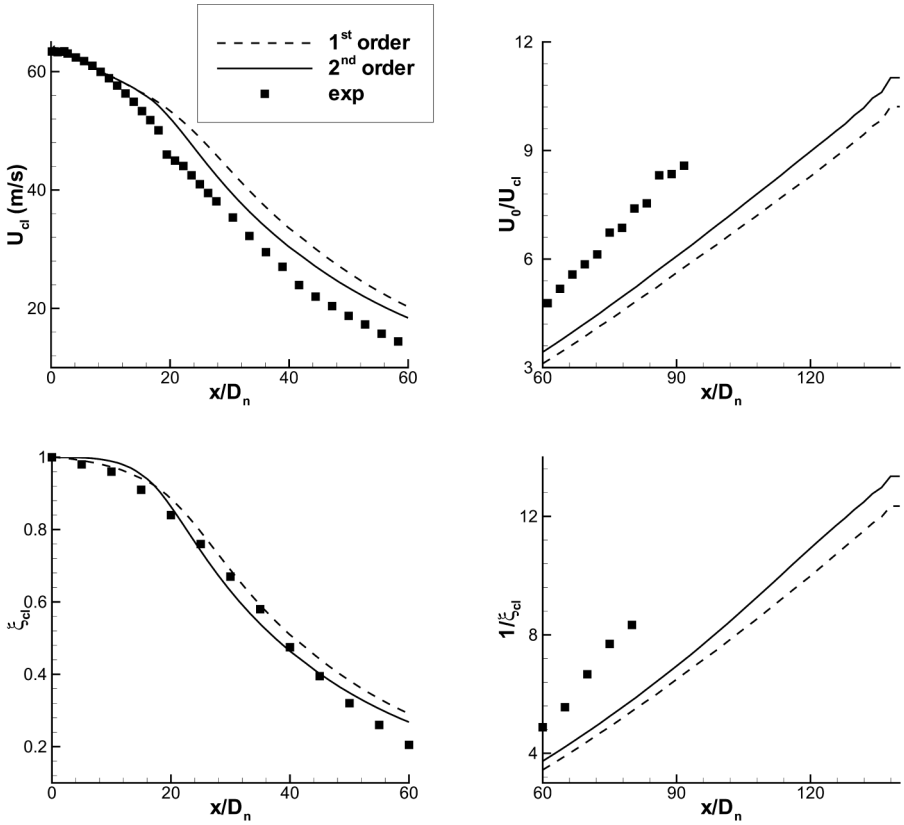

Figure 1.
Axial profiles of the mean velocity and mixture fraction

numerical viscosity affects the results. In Figure 2 (right), a measure for the numerical viscosity (9) is shown. For h, the radial grid spacing at the axis is taken, while the local mean axial velocity is used for U. This diffusion is in the axial direction, where convection is dominant. Still, it is indicative that the numerical viscosity is not negligible, particularly for small values of x (say $x < 20D_n$). This is seen in the profiles of ρk. In Merci *et al.* (2001) it is demonstrated that the decay in mean velocity is governed by the turbulent shear stress at the symmetry axis, and that ρk is a good measure for this quantity. In Figure 2, a completely different behaviour is observed when a first- or a second-order accurate scheme is applied. Due to the large amount of numerical dissipation for small x, the turbulent shear stress does not increase as quickly as with the second-order scheme. As a result, the decay of the mean velocity (and thus of the mean mixture fraction) is postponed, as show in Figure 1. This is reflected in a serious discrepancy in the prediction of the position of stoichiometric conditions (Table I). There are also differences in the final decay, due to differences in the values for the eddy viscosity (Figure 2). It is noteworthy that the decay is slightly steeper with the second-order scheme than with the first-order discretization, in contrast to the higher numerical diffusion in the latter. The reason is found in different evolution of the eddy viscosity, which dominates the numerical diffusion in that region and which is higher with the second-order scheme (Figure 2). To conclude, it is noted that the difference in the behaviour of ρk is also observed in the axial profiles for the mixture fraction variance, which is shown in Figure 3; the increase is postponed when a first-order accurate scheme is used.

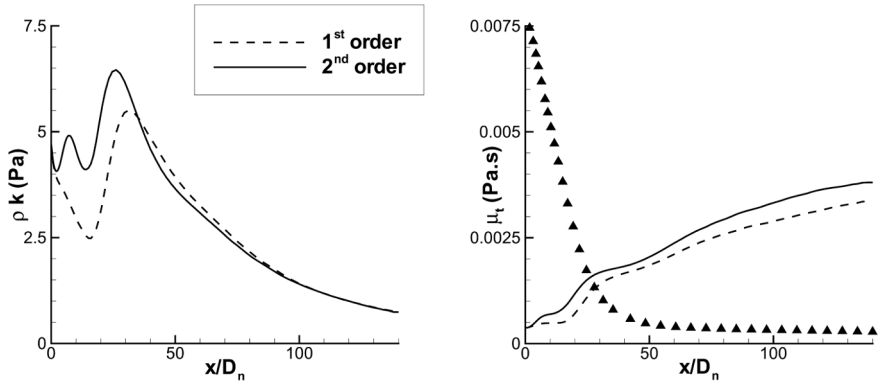

Figure 2.
Axial profiles of ρk (left) and the eddy viscosity (right). Symbols: μ_{num} (equation (9))

Table I.
Position of stoichiometric conditions at the axis

Model	First-order	Second-order	Exp.
x_{st}/D_n	53.2	49.7	47 ± 2.3

Figures 4 and 5 show the radial profiles at $x/D_n = 30$ and $x/D_n = 45$ for the mean velocity, mixture fraction and temperature, and for the rms value of the mixture fraction fluctuations. The radial "shape" is presented for these quantities: they are divided by their value at the centerline at the considered

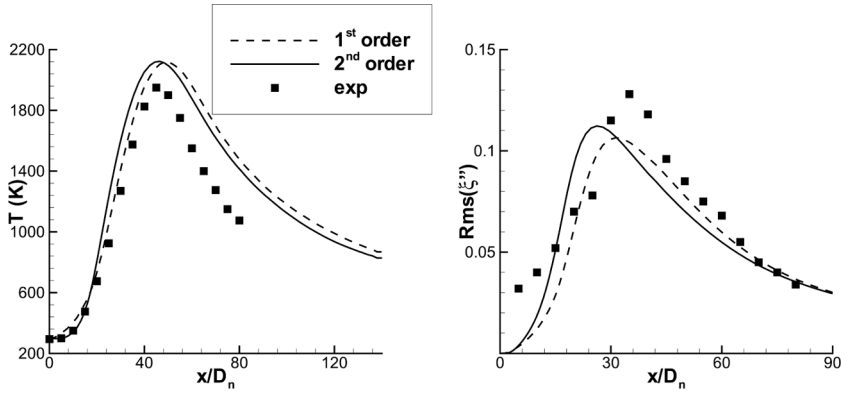

Figure 3.
Axial profiles of mean temperature (left) and the rms value of the mixture fraction fluctuations (right)

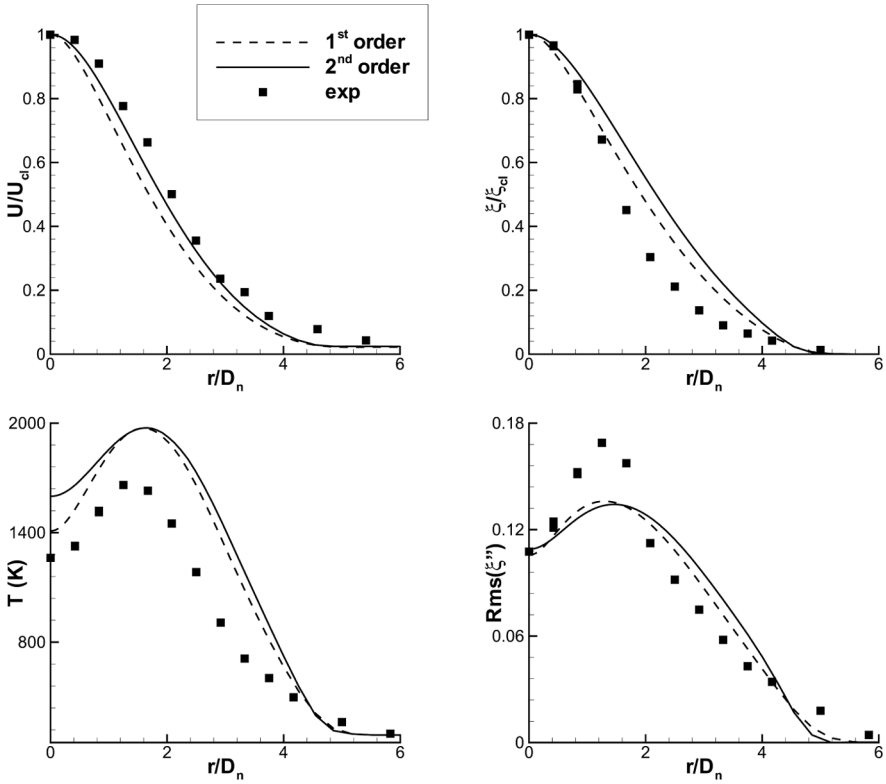

Figure 4.
Radial profiles at $x/D_n = 30$

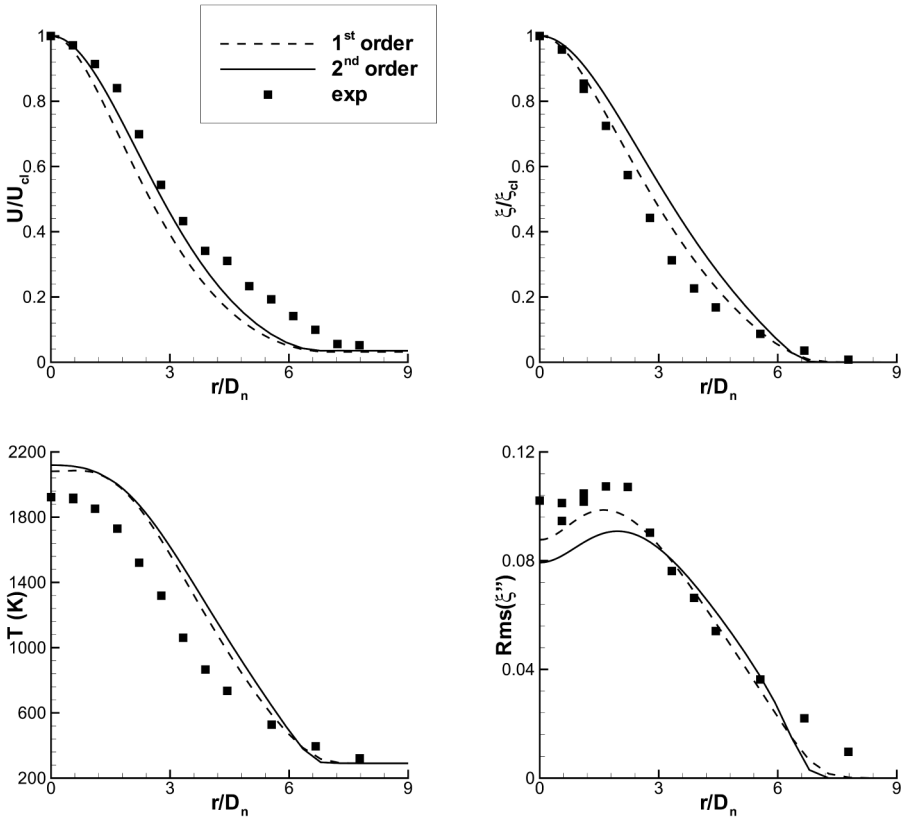

Figure 5.
Radial profiles at $x/D_n = 45$

axial position. Again, large discrepancies are observed when the order of accuracy of the numerical scheme is altered: there is a clear difference in the spreading rates for both U and ξ. Therefore, it is dangerous to claim (see http://www.ca.sandia.gov/tdf/Workshop/Submodels.html) that the value $c_{\varepsilon 2} = 1.8$ provides a correct spreading rate, without specification of the applied numerical scheme. The profiles for the mean temperature reveal the large differences even more. In Figure 4, a temperature difference of 180 K is observed at the axis, while the larger spreading rate with the second-order accurate scheme is also seen in Figure 5. For the mixture fraction variance, the differences are not negligible, either, which is best seen in Figure 5. It is noteworthy that the spreading rate with the second-order scheme is larger than with the first-order accuracy, in contrast to the higher numerical diffusion with the latter. The reason is again found in the differences in the eddy viscosity.

5.2 Boundary conditions

The influence of the inlet boundary conditions is very large, as discussed in Merci *et al.* (2002). Since the complete discussion has been done in that

reference, attention is focused onto the outlet boundary conditions. Although they are straightforward (prescribed atmospheric static pressure and zero axial derivatives for all other quantities), it is possible that the results are affected if the axial derivatives in reality differ from zero at the position of the outlet boundary. Figures 6 and 7 show that this is not the case. It is observed that moving the outlet boundary from $x = 140D_n$ closer to the nozzle exit ($x = 80D_n$), does not affect the simulation results upstream. All profiles indeed collapse. Consequently, it is not necessary to use a very large computational grid.

5.3 Grid refinement

In Figure 8, axial profiles are shown for first- and second-order accurate results on the basic grid (113×89 points) and on a refined grid (225×89 points). Clearly, the second-order accurate results are grid independent (all curves practically collapse). Although the first-order accurate results are also at first sight grid independent, this is not completely true. As mentioned earlier, the

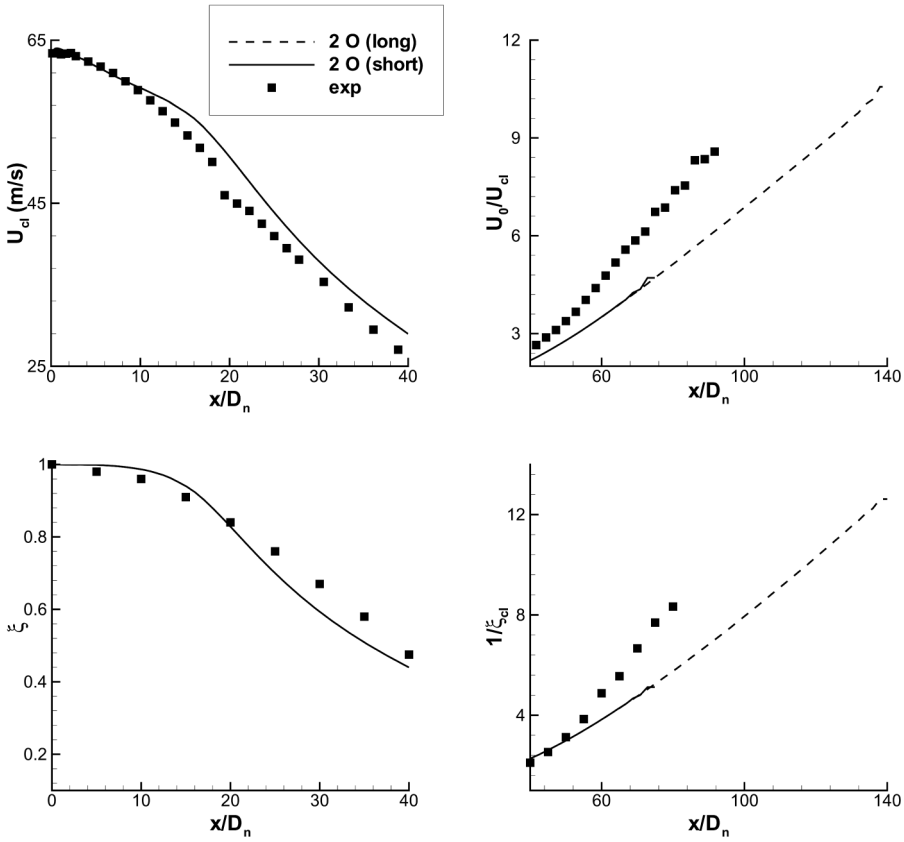

Figure 6.
Comparison of axial profiles for the basic grid ($140D_n \times 25D_n$) and a shortened grid ($80D_n \times 25D_n$)

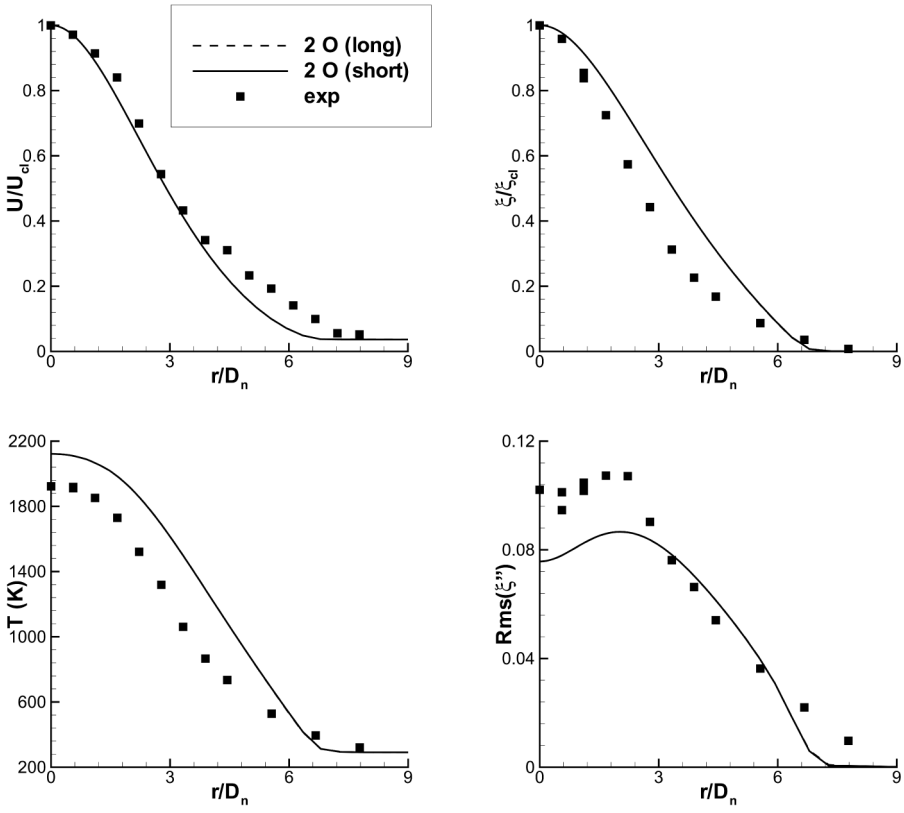

Figure 7.
Comparison of radial profiles at $x/D_n = 45$ for the basic grid ($140D_n \times 25D_n$) and a shortened grid ($80D_n \times 25D_n$)

numerical viscosity (9) is important in the first-order accurate simulations (Figure 3). Consequently, the influence of grid refinement is visible, particularly in the profile for ρk, which is the most sensitive. It is seen that the profile on the refined grid starts to tend toward the grid independent curve of the second-order accurate scheme, since the numerical viscosity is divided by a factor of two (equation (9)), where h is divided by two due to the grid refinement). Although it is hardly visible, the other profiles also tend towards the second-order profiles. Thus, the explanation of the differences between the first- and second-order scheme in Figures 1 and 2 as described earlier, which were based on Figure 3, are supported by the observations in Figure 8. To conclude, it is noted that, in order to obtain really grid independent results with a first-order accurate scheme, the grid must be much more refined than the second-order scheme. However, the variations in the other curves in Figure 8 are small, so that the results seem grid independent (and are often claimed to be so), although they are really not. To judge on grid independence, sensitive quantities have to be observed.

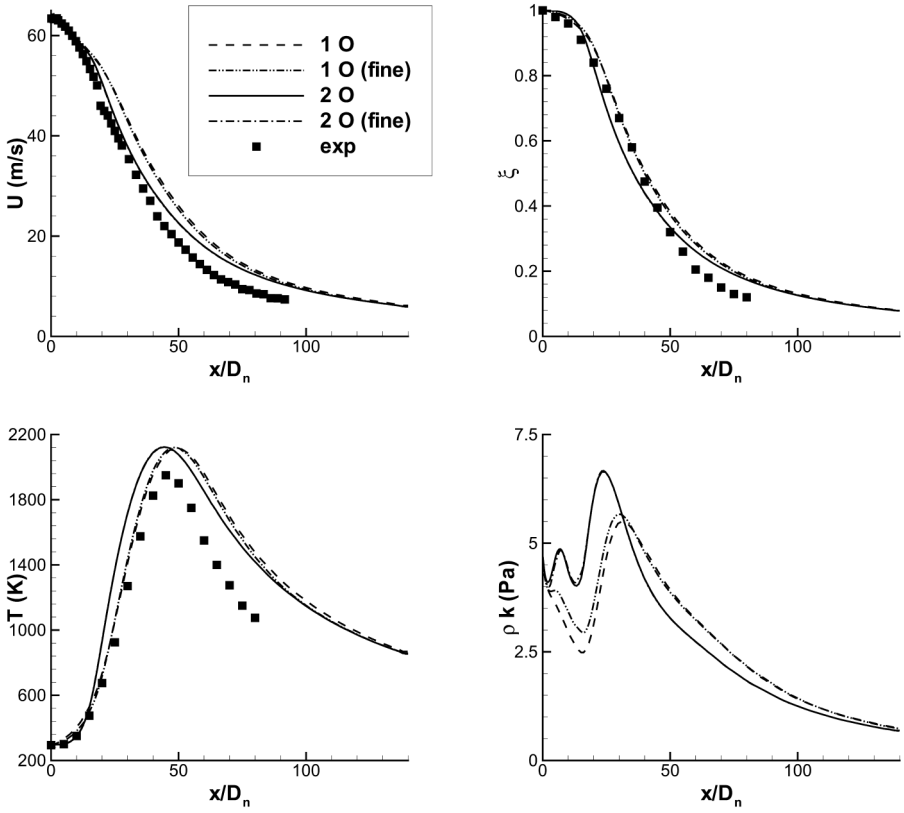

Figure 8.
Comparison of axial profiles for the basic grid (113 × 89 points) and a refined grid (225 × 177 points)

6. Conclusions

The influence of computational aspects on numerical simulations was quantitatively investigated for a turbulent piloted jet diffusion flame. The inlet boundary conditions, particularly for the dissipation rate ε, are of crucial importance to obtain the reliable results (Merci *et al.*, 2002).

Apart from the inlet boundary conditions, the order of accuracy of the numerical scheme has a large impact on the calculation results, both in terms of axial and radial flame structure. It is important to use a sufficiently accurate spatial discretization, in order not to affect the simulation results through uncontrolled artificial numerical dissipation.

Unlike the inlet boundary conditions, the outlet boundary (in particular, its axial position) has very little effect on the simulation results.

It has been demonstrated that care must be taken when results are claimed to be grid independent. In particular, first-order accurate results may seem grid independent when the grid is refined by a factor of two, when relatively insensitive quantities are investigated. In reality, they are not grid independent,

unless an extremely fine grid is employed. Results obtained with a second-order accurate scheme, on the other hand, have been shown to be really grid independent.

References

Barlow, R.S. and Frank, J.H. (1998), "Effects of turbulence on species mass fractions in methane/air jet flames", *Proceedings of The Combustion Institute*, Vol. 27, pp. 1087-95, (Data also available on: www.ca.sandia.gov/tdf/Workshop.html).

Bilger, R.W. and Starner, S.H. (1983), "A simple model for carbon monoxide in laminar and turbulent hydrocarbon diffusion flames", *Combustion and Flame*, Vol. 51, pp. 155-76.

Jones, W.P. (1994), "Turbulence modelling and numerical solution methods", in Libby, P.A. and Williams, F.A. (Eds), *Turbulent Reacting Flows*, Academic Press, London, pp. 309-74.

Jones, W.P. and Launder, B.E. (1972), "The prediction of laminarization with a two-equation model of turbulence", *AIAA Journal*, Vol. 15, pp. 301-14.

Merci, B., Dick, E., Vierendeels, J. and De Langhe, C. (2002), "Determination of ε at inlet boundaries", *International Journal of Numerical Methods for Heat and Fluid Flow*, Vol. 12 No. 1, pp. 65-80.

Merci, B., Dick, E., Vierendeels, J., Roekaerts, D. and Peeters, T.W.J. (2001), "Application of a new cubic turbulence model to piloted and bluff-body diffusion flames", *Combustion and Flame*, Vol. 126 No. 1/2, pp. 1533-56.

Merci, B., Steelant, J., Vierendeels, J., Riemslagh, K. and Dick, E. (2000), "Computational treatment of source terms in two-equation turbulence models", *AIAA Journal*, Vol. 38 No. 11, pp. 2085-93.

Pope, S.B. (2000), *Turbulent flows*, Cambridge University Press, Cambridge.

Vierendeels, J., Merci, B. and Dick, E. (2001), "A blended AUSM+ method for all speeds and all grid aspect ratios", *AIAA Journal*, Vol. 39 No. 12, pp. 2278-82.